One- and two-photon absorption properties of diamond nitrogen-vacancy defect centers: A theoretical study

Chih-Kai Lin, Yi-Hsieh Wang, Huan-Cheng Chang, M. Hayashi, and S. H. Lin

Articles you may be interested in

Optical manipulation of the charge state of nitrogen-vacancy center in diamond
Appl. Phys. Lett. 103, 013112 (2013); 10.1063/1.4813120

Theoretical study of one- and two-photon absorption spectra of azoaromatic compounds
J. Chem. Phys. 131, 244516 (2009); 10.1063/1.3271239

Theoretical study of one-photon and two-photon absorption properties of perylene tetracarboxylic derivatives
J. Chem. Phys. 129, 014301 (2008); 10.1063/1.2938374

Vibronic induced one- and two-photon absorption in a charge-transfer stilbene derivate
J. Chem. Phys. 126, 244509 (2007); 10.1063/1.2745794

Theoretical investigation of two-photon absorption allowed excited states in symmetrically substituted diacetylenes by ab initio molecular-orbital method
J. Chem. Phys. 124, 124303 (2006); 10.1063/1.2181973

One- and two-photon absorption properties of diamond nitrogen-vacancy defect centers: A theoretical study

Chih-Kai Lin,[1,2,a)] Yi-Hsieh Wang,[1] Huan-Cheng Chang,[1] M. Hayashi,[3] and S. H. Lin[1,4]

[1]*Institute of Atomic and Molecular Sciences, Academia Sinica, Taipei, Taiwan 10617, Republic of China*
[2]*Taiwan International Graduate Program, Department of Chemistry, National Tsing Hua University, Hsinchu, Taiwan 30013, Republic of China*
[3]*Center for Condensed Matter Sciences, National Taiwan University, Taipei, Taiwan 10617, Republic of China*
[4]*Department of Applied Chemistry, National Chiao Tung University, Hsinchu, Taiwan 30010, Republic of China*

The negatively charged nitrogen-vacancy defect center, $(NV)^-$, in diamond has been investigated theoretically for its one- and two-photon absorption properties involving the first excited state with the $^3A_2 \rightarrow {}^3E$ transition. Time-dependent density functional theory (TD-DFT), configuration interaction with single excitation (CIS), and complete active space self-consistent field (CASSCF) were employed in this investigation along with the 6-31G(d) basis set. Diamond lattice models containing 24–104 carbon atoms were constructed to imitate the local environment of the defect center. TD-DFT calculations in large molecular cluster models (with 85 or more carbon atoms) predicted the vertical excitation energy quite consistent with the experimental absorption maximum. CASSCF calculations were feasible only for small cluster models (less than 50 carbon atoms) but yielded one-photon absorption (OPA) and two-photon absorption (TPA) cross sections somewhat larger than the experimental values obtained with linearly polarized incident light [T.-L. Wee *et al.*, J. Phys. Chem. A **111**, 9379 (2007)]. CIS calculations in larger cluster models showed a systematic overestimation of the excitation energy while just slightly underestimated the OPA cross section and overestimated the TPA cross section. The agreements between calculations and measurements suggest that the computational approaches established in this work are applicable to explore the optical properties of related defect centers in diamond as well. © *2008 American Institute of Physics*. [DOI: 10.1063/1.2987717]

I. INTRODUCTION

The diamond nitrogen-vacancy defect center that emits extended red emission peaking at ∼700 nm was first identified in the 1970s.[1] The centers can be found in type Ib diamonds bombarded by high-energy particles, e.g., electrons or protons of several MeV in energy, followed by annealing at temperature ∼900 °C.[1,3] Through three decades of experimental studies, properties such as absorption and emission spectroscopy, geometrical structure, electronic configuration, etc., of this defect center have been widely characterized.[4–15] It is now known that the center is composed of a single substitutional nitrogen atom and a neighboring vacancy plus an extra negative charge, hence denoted as $(NV)^-$, bearing the C_{3v} symmetry. The characteristic zero-phonon line (ZPL) at 637 nm (1.945 eV) is corresponding to the $^3A_2 \leftrightarrow {}^3E$ transition, along with a broad vibronic sidebands in both absorption and fluorescence spectra.[1–3,11–13,15] At least one $^1A_1$ state was suggested locating between the two triplet states, which could grasp certain population and lead to reduction in fluorescence intensity and spin polarization during continuous excitation-emission events.[10,13,14]

In the theoretical regime, a number of potential models have been proposed to simulate the observed spectra.[1,16,17] *Ab initio* and semiempirical calculations, on the other hand, have been carried out to clarify the structure, excitation energies and sequence of states, spin features and hyperfine tensors, etc.[18,22] Either large model clusters[18,20,22] or supercells[19,21] were applied in these calculations. Vertical excitation energies obtained using density functional theory (DFT) with the BP functional or with the local density approximation (LDA), in cooperation with the ΔSCF method, were found tentatively comparable to experimental measurements.[18,21,22]

This work was motivated by our recent studies and demonstrations that nanometer-sized diamond particles containing $(NV)^-$ centers are useful as fluorescent biomarkers for *in vitro* imaging applications.[23–25] These particles, named fluorescent nanodiamonds (FNDs), possess several unique properties such as good biocompatibility, excellent photostability, and facile surface functionalizability. Because of the low cytotoxicity of the matrix and the nonphotobleaching characteristic of the defect center, FNDs are well suited for long-term imaging and tracking in live cells by fluorescence microscopy.[26] When the surface is further modified with bio-

a)Electronic mail: ethene@gate.sinica.edu.tw.

molecules, these particles may serve as drug or gene carriers for targeted diagnosis and therapy.[27–29]

A topic of fundamental interest in FND is the intrinsic spectroscopic property of the defect centers it contains. The photoluminescence quantum efficiency of the $(NV)^-$ center upon the $^3A_2 \rightarrow {}^3E$ excitation is near unity,[7,8] and therefore the brightness of the resulting fluorescence in one-photon excitation is proportional to the absorption cross section. Recently, Wee *et al.*[30] performed measurements on both one- and two-photon absorption cross sections of this defect center, based on the concentration estimated from the integrated absorption coefficient of the ZPL for diamond single crystals.[31,32] In the case of one-photon absorption (OPA), they determined a cross section of $\sigma_{OPA} = (3.1 \pm 0.8) \times 10^{-17}$ cm^2 at 532 nm using absorption spectroscopy.[30] For the two-photon absorption (TPA), while the cross section is too small to be measured directly by absorption spectroscopy, it was determined by laser-induced fluorescence measurements. This was accomplished by measuring the relative strength of two-photon versus one-photon excited emissions and comparing the intensity ratio with that of molecular fluorophores such as rhodamine B whose σ_{OPA} and σ_{TPA} are known under the same experimental conditions. At 1064 nm, a TPA cross section of $\sigma_{TPA} = (0.45 \pm 0.23) \times 10^{-50}$ cm^4 s for the $(NV)^-$ center was determined. Such a σ_{TPA} value is about 30 times as small as that of rhodamine B at the same excitation wavelength; however, this deficit can readily be compensated by increasing the concentration of defect centers in each FND particle.[30]

This article presents a theoretical study on the spectroscopic characteristics of the $(NV)^-$ center based on *ab initio* calculations. The calculations were performed using configuration interaction with single excitation (CIS), complete active space self-consistent field (CASSCF), and time-dependent density functional theory (TD-DFT) to estimate σ_{OPA}, σ_{TPA}, and related properties. Since it is impractical to compute a diamond lattice of macroscopic size, we chose to model the system with small-sized clusters (or large diamondoids) containing up to about 100 carbon atoms. Calculated excitation energies and absorption cross sections were then compared to experimental results.

II. THEORY

A. One-photon absorption

According to the Fermi golden rule, the transition from the initial electronic state i to the final state f in the OPA process can be written as[33,34]

$$W_{i \rightarrow f}^{(1)}(\omega) = \frac{2\pi}{\hbar^2} |\boldsymbol{\mu}_{fi} \cdot \mathbf{E}_0(\omega)|^2 \sum_v \sum_{v'} P_{iv} |\langle \Theta_{fv'} | \Theta_{iv} \rangle|^2 \times D(\omega_{fv',iv} - \omega, \gamma_{fv',iv}), \quad (1)$$

where v and v' are vibrational quantum numbers of the electronic states i and f, respectively, ω is the excitation angular frequency, $\omega_{fv',iv}$ is the angular frequency corresponding to the adiabatic transition energy between the two stationary states iv and fv', P is the Boltzmann distribution factor, $\boldsymbol{\mu}$ is the electronic transition dipole moment vector, $\mathbf{E}_0$ is the am-

plitude vector of the incident sinusoidal electric field, $|\langle \Theta_{fv'} | \Theta_{iv} \rangle|^2$ is the Franck–Condon factor, and $D(\Delta\omega, \gamma)$ is the Lorentzian lineshape function with the dephasing constant γ in the form of

$$D(\Delta\omega, \gamma) = \frac{1}{\pi} \frac{\gamma}{(\Delta\omega)^2 + \gamma^2}. \quad (2)$$

Taking orientational averages of the light-matter interaction in three dimensions leads to

$$\langle W_{i \rightarrow f}^{(1)}(\omega) \rangle = \frac{2\pi}{3\hbar^2} |\boldsymbol{\mu}_{fi}|^2 |\mathbf{E}_0(\omega)|^2 \sum_v \sum_{v'} P_{iv} |\langle \Theta_{fv'} | \Theta_{iv} \rangle|^2 \times D(\omega_{fv',iv} - \omega, \gamma_{fv',iv}). \quad (3)$$

In the cases that the temperature is low, most molecules are populated at the lowest vibrational level, i.e., $P_{iv} \approx 1$ for $v = 0$ and $P_{iv} \approx 0$ otherwise. Equation (3) can then be approximated as

$$\langle W_{i \rightarrow f}^{(1)}(\omega) \rangle \approx \frac{2\pi}{3\hbar^2} |\boldsymbol{\mu}_{fi}|^2 |\mathbf{E}_0(\omega)|^2 \sum_{v'} |\langle \Theta_{fv'} | \Theta_{i0} \rangle|^2 \times D(\omega_{fv',i0} - \omega, \gamma_{fv',i0}). \quad (4)$$

The OPA cross section of the transition has a form of

$$\sigma_{OPA}(\omega) = \frac{\langle W_{i \rightarrow f}^{(1)}(\omega) \rangle \cdot \hbar\omega}{I \cdot n_e(\omega)}$$

$$= \frac{4\pi^2 \omega}{3\hbar c n_e(\omega)} |\boldsymbol{\mu}_{fi}|^2 \sum_{v'} |\langle \Theta_{fv'} | \Theta_{i0} \rangle|^2 \times D(\omega_{fv',i0} - \omega, \gamma_{fv',i0}), \quad (5)$$

where n_e is the frequency-dependent refractive index of the medium and I is the intensity of the incident light,

$$I = \frac{c}{2\pi} |\mathbf{E}_0(\omega)|^2. \quad (6)$$

If all parameters are expressed in atomic units, Eq. (5) becomes

$$\sigma_{OPA}(\omega) = \frac{4\pi^2 \alpha \omega}{3 n_e(\omega)} |\mathbf{R}_{fi}|^2 \sum_{v'} |\langle \Theta_{fv'} | \Theta_{i0} \rangle|^2 \times D(\omega_{fv',i0} - \omega, \gamma_{fv',i0}), \quad (7)$$

where $\alpha = 7.297 \times 10^{-3}$ is the fine structure constant, and $\mathbf{R}$ is the transition moment depicted as a spatial vector.

B. Two-photon absorption

In the TPA process, given the two photons have angular frequencies of ω_λ and ω_κ, respectively, the rate of the transition from the initial state i to the final state f is[34]

$$W_{i \rightarrow f}^{(2)}(\omega_\lambda, \omega_\kappa) = \frac{2\pi}{\hbar^2} |M_{fi}(\omega_\lambda, \omega_\kappa)|^2 \sum_v \sum_{v'} P_{iv} |\langle \Theta_{fv'} | \Theta_{iv} \rangle|^2 \times D(\omega_{fv',iv} - \omega_\lambda - \omega_\kappa, \gamma_{fv',iv}), \quad (8)$$

where M_{fi} denotes the two-photon transition matrix element tensor,

$$M_{fi}(\omega_\lambda, \omega_\kappa) = \sum_m \left\{ \frac{(\boldsymbol{\mu}_{fm} \cdot \mathbf{E}_\lambda)(\boldsymbol{\mu}_{mi} \cdot \mathbf{E}_\kappa)}{\hbar(\omega_{mi} - \omega_\kappa)} \right.$$

$$\left. + \frac{(\boldsymbol{\mu}_{fm} \cdot \mathbf{E}_\kappa)(\boldsymbol{\mu}_{mi} \cdot \mathbf{E}_\lambda)}{\hbar(\omega_{mi} - \omega_\lambda)} \right\}$$

$$= \frac{e^2 |\mathbf{E}_\lambda||\mathbf{E}_\kappa|}{\hbar} \sum_m \left\{ \frac{(\mathbf{R}_{fm} \cdot \boldsymbol{\lambda})(\mathbf{R}_{mi} \cdot \boldsymbol{\kappa})}{\omega_{mi} - \omega_\kappa} \right.$$

$$\left. + \frac{(\mathbf{R}_{fm} \cdot \boldsymbol{\kappa})(\mathbf{R}_{mi} \cdot \boldsymbol{\lambda})}{\omega_{mi} - \omega_\lambda} \right\}$$

$$= \frac{e^2 |\mathbf{E}_\lambda||\mathbf{E}_\kappa|}{\hbar} S_{fi}^{\kappa\lambda}(\omega_\lambda, \omega_\kappa), \tag{9}$$

where $\boldsymbol{\mu}$ is the electronic transition dipole moment and $\mathbf{R}$ is the corresponding spatial vector, $\boldsymbol{\lambda}$ and $\boldsymbol{\kappa}$ are polarization vectors of the radiations, $\mathbf{E}_\lambda$ and $\mathbf{E}_\kappa$ are the amplitude vectors of incident sinusoidal electric fields, respectively, and the term

$$S_{fi}^{\kappa\lambda}(\omega_\lambda, \omega_\kappa) = \sum_A^{X,Y,Z} \sum_B^{X,Y,Z} \sum_a^{x,y,z} \sum_b^{x,y,z} \kappa_B \lambda_A \xi_{Aa} \xi_{Bb}$$

$$\times \sum_m \left(\frac{R_{fm}^b R_{mi}^a}{\omega_{mi} - \omega_\lambda} + \frac{R_{fm}^a R_{mi}^b}{\omega_{mi} - \omega_\kappa} \right) \tag{10}$$

is a transformed two-photon transition matrix element tensor, which projects the transition dipole moments from the molecular frame (x, y, z) onto the laboratory frame (X, Y, Z) through the transformation matrices ξ's. Note that in Eq. (9), the sum is carried out over all possible intermediate states m's, including initial $(m=i)$ and final $(m=f)$ states themselves in the case of noncentrosymmetric systems.[35,37] The vibrational levels are not included in the calculation, assuming that the energy gap between the electronic states is much larger than that between the pure vibrational states, i.e., the Placzek approximation. Taking the orientational average on the square of the transformed matrix element yields[34,38]

$$\langle |S_{fi}^{\kappa\lambda}(\omega_\lambda, \omega_\kappa)|^2 \rangle = \frac{1}{30} \sum_a^{x,y,z} \sum_b^{x,y,z} (F S_{fi}^{aa} S_{fi}^{bb*} + G S_{fi}^{ba} S_{fi}^{ba*}$$

$$+ H S_{fi}^{ba} S_{fi}^{ab*}), \tag{11}$$

where

$$S_{fi}^{ba}(\omega_\lambda, \omega_\kappa) = \sum_m \left(\frac{R_{fm}^b R_{mi}^a}{\omega_{mi} - \omega_\lambda} + \frac{R_{fm}^a R_{mi}^b}{\omega_{mi} - \omega_\kappa} \right) \tag{12}$$

and a and b denoted x, y, or z, respectively. The values of the three parameters F, G, and H in Eq. (11) depends on the polarizations as well as incident angles of the excitation photons involved in the TPA process. For example, $(F, G, H) = (2, 2, 2)$ when both photons are linearly polarized with parallel propagation and $(F, G, H) = (-2, 3, 3)$ when both photons are circularly polarized with parallel propagation.[34] In the low-temperature case, the orientation-averaged TPA transition rate can be written as

$$\langle W_{i \to f}^{(2)}(\omega_\lambda, \omega_\kappa) \rangle \approx \frac{2\pi}{\hbar^2} \langle |M_{fi}(\omega, \omega)|^2 \rangle \sum_{v'} |\langle \Theta_{fv'} | \Theta_{i0} \rangle|^2$$

$$\times D(\omega_{fv',i0} - \omega_\lambda - \omega_\kappa, \gamma_{fv',i0})$$

$$= \frac{\pi e^4 |\mathbf{E}_\lambda|^2 |\mathbf{E}_\kappa|^2}{15\hbar^4} \sum_a \sum_b [F S_{fi}^{aa} S_{fi}^{bb*} + G S_{fi}^{ba} S_{fi}^{ba*}$$

$$+ H S_{fi}^{ba} S_{fi}^{ab*}] \sum_{v'} |\langle \Theta_{fv'} | \Theta_{i0} \rangle|^2$$

$$\times D(\omega_{fv',i0} - \omega_\lambda - \omega_\kappa, \gamma_{fv',i0}) \tag{13}$$

and the corresponding TPA cross section is

$$\sigma_{\text{TPA}}(\omega_\lambda, \omega_\kappa) = \frac{\langle W_{i \to f}^{(2)}(\omega_\lambda, \omega_\kappa) \rangle \cdot \hbar^2 \omega_\lambda \omega_\kappa}{I_\lambda n_e(\omega_\lambda) \cdot I_\kappa n_e(\omega_\kappa)}$$

$$= \frac{4\pi^3 e^4 \omega_\lambda \omega_\kappa}{15\hbar^2 c^2 n_e(\omega_\lambda) n_e(\omega_\kappa)} \sum_a \sum_b [F S_{fi}^{aa} S_{fi}^{bb*}$$

$$+ G S_{fi}^{ba} S_{fi}^{ba*} + H S_{fi}^{ba} S_{fi}^{ab*}] \sum_{v'} |\langle \Theta_{fv'} | \Theta_{i0} \rangle|^2$$

$$\times D(\omega_{fv',i0} - \omega_\lambda - \omega_\kappa, \gamma_{fv',i0}) \tag{14}$$

or

$$\sigma_{\text{TPA}}(\omega_\lambda, \omega_\kappa) = \frac{4\pi^3 \alpha^2 \omega_\lambda \omega_\kappa}{15 n_e(\omega_\lambda) n_e(\omega_\kappa)} \sum_a \sum_b [F S_{fi}^{aa} S_{fi}^{bb*}$$

$$+ G S_{fi}^{ba} S_{fi}^{ba*} + H S_{fi}^{ba} S_{fi}^{ab*}] \sum_{v'} |\langle \Theta_{fv'} | \Theta_{i0} \rangle|^2$$

$$\times D(\omega_{fv',i0} - \omega_\lambda - \omega_\kappa, \gamma_{fv',i0}) \tag{15}$$

in atomic units.

In the case of single-beam one-color TPA process, the expression is slightly different. The transition matrix element tensors in Eqs. (9) and (11) become

$$M_{fi}(\omega, \omega) = \sum_m \frac{(\boldsymbol{\mu}_{fm} \cdot \mathbf{E}_0)(\boldsymbol{\mu}_{mi} \cdot \mathbf{E}_0)}{\hbar(\omega_{mi} - \omega)}$$

$$= \frac{e^2 |\mathbf{E}_0|^2}{\hbar} \sum_m \frac{(\mathbf{R}_{fm} \cdot \boldsymbol{\lambda})(\mathbf{R}_{mi} \cdot \boldsymbol{\lambda})}{\omega_{mi} - \omega}$$

$$= \frac{e^2 |\mathbf{E}_0|^2}{\hbar} S_{fi}^{\lambda\lambda}(\omega, \omega) \tag{16}$$

and

$$\langle |S_{fi}^{\lambda\lambda}(\omega, \omega)|^2 \rangle = \frac{1}{120} \sum_a \sum_b (F S_{fi}^{aa} S_{fi}^{bb*} + G S_{fi}^{ba} S_{fi}^{ba*}$$

$$+ H S_{fi}^{ba} S_{fi}^{ab*}), \tag{17}$$

where

$$S_{fi}^{ba}(\omega, \omega) = S_{fi}^{ab}(\omega, \omega) = \sum_m \left(\frac{R_{fm}^b R_{mi}^a}{\omega_{mi} - \omega} + \frac{R_{fm}^a R_{mi}^b}{\omega_{mi} - \omega} \right) \tag{18}$$

and, therefore,

$$\langle W_{i \to f}^{(2)}(\omega,\omega) \rangle = \frac{\pi e^4 |\mathbf{E}_0|^4}{30\hbar^4} \sum_a \sum_b (F S_{fi}^{aa} S_{fi}^{bb*} + 2 G S_{fi}^{ab} S_{fi}^{ab*})$$

$$\times \sum_{v'} |\langle \Theta_{fv'} | \Theta_{i0} \rangle|^2 D(\omega_{fv',i0} - 2\omega, \gamma_{fv',i0}).$$

$$(19)$$

The corresponding TPA cross section in atomic units becomes

$$\sigma_{\text{TPA,linear}}(\omega,\omega) = 2 \frac{\langle W_{i \to f}^{(2)}(\omega,\omega) \rangle \cdot \hbar^2 \omega^2}{I^2 n_e^2(\omega)}$$

$$= \frac{4\pi^3 \alpha^2 \omega^2}{15 n_e^2(\omega)} \sum_a \sum_b [S_{fi}^{aa} S_{fi}^{bb*} + 2 S_{fi}^{ab} S_{fi}^{ab*}]$$

$$\times \sum_{v'} |\langle \Theta_{fv'} | \Theta_{i0} \rangle|^2$$

$$\times D(\omega_{fv',i0} - 2\omega, \gamma_{fv',i0}) \qquad (20)$$

for linearly polarized light and

$$\sigma_{\text{TPA,circular}}(\omega,\omega) = \frac{4\pi^3 \alpha^2 \omega^2}{15 n_e^2(\omega)} \sum_a \sum_b [- S_{fi}^{aa} S_{fi}^{bb*} + 3 S_{fi}^{ab} S_{fi}^{ab*}]$$

$$\times \sum_{v'} |\langle \Theta_{fv'} | \Theta_{i0} \rangle|^2$$

$$\times D(\omega_{fv',i0} - 2\omega, \gamma_{fv',i0}) \qquad (21)$$

for circularly polarized light. Note that in Eq. (20), the multiplication factor of 2 is derived because the amount of absorption is measured with the dissipation rate of the incident photons, which is twice the transition rate in a single-beam TPA setup.[39,40]

III. COMPUTATIONAL METHODS

Several model clusters (or large diamondoids) have been constructed to simulate the local environment of the nitrogen-vacancy defect center in the diamond lattice. The smallest one, denoted as $C_{24}(NV)^- H_{30}$, is composed of 24 carbon atoms, one substitutional nitrogen atom, one substitutional vacancy adjacent to the nitrogen atom, 30 terminal hydrogen atoms passivating the cluster surface, and one extra negative charge. Further increasing the number of carbon atoms around the defect center led to $C_{33}(NV)^- H_{36}$, $C_{49}(NV)^- H_{52}$, $C_{85}(NV)^- H_{76}$, $C_{89}(NV)^- H_{80}$, and $C_{104}(NV)^- H_{76}$. They have disk-, cube-, tetrahedron-, or sphere-like structures, respectively, as depicted in Fig. 1. The largest cluster can be regarded as a hydrogenated nanodiamond particle with a diameter of ~ 1.2 nm. Studies on even larger clusters were not attempted here because of limitation in computational resources.

The structures of all model clusters were first optimized, followed by computations for their spectroscopic properties including vertical excitation energies, transition dipole moments, etc. Two different methods have been employed in the calculations: (1) Hartree–Fock self-consistent field (HF-SCF) which was used to optimize the ground state structure and CISs and/or CASSCF (or CAS for short) computations fol-
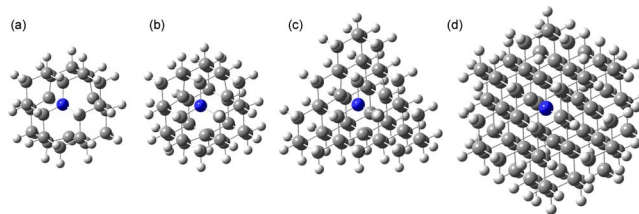

FIG. 1. (Color online) Several hydrogenated diamondoids containing $(NV)^-$ defect centers used in the calculations: (a) Disklike $C_{24}(NV)^- H_{30}$, (b) cuboidlike $C_{33}(NV)^- H_{36}$, (c) tetrahedron-like $C_{49}(NV)^- H_{52}$, and (d) sphere-like $C_{85}(NV)^- H_{76}$. In each model the nitrogen atom is located at the center, and the carbon cluster surface is passivated with hydrogen atoms.

lowed to characterize the excited states. (2) DFT in which the ground state structure was optimized using the B3LYP functional and the corresponding excited states were calculated using TD-DFT. The widely used 6-31G(d) basis set was applied; the diffuse function was sometimes introduced additionally to investigate the basis set dependence. All the TD-DFT and CIS computations were performed with the GAUSSIAN 03 package,[41] and the CASSCF computations were carried out additionally using the MOLPRO package.[42]

Preliminary results showed that all the optimized ground state structures were diamondlike while nonsignificant structural distortions unavoidably occur around the defect center, similar to those reported previously.[20–22] The spin densities distributed mainly and equally on the three carbon atoms surrounding the vacancy with a value of ~ 0.6 to 0.7 while virtually zero was found on the nitrogen atom, in consistent with former reports.[19–21] Moreover, the electronic configurations of the highest occupied molecular orbital (HOMO) and nearby levels were generally the same, irrespective of the sizes of the model clusters and computational settings used. As shown in Fig. 2, the ground state has two unpaired α-spin electrons in the doubly degenerate HOMO, labeled with $^3A_2$. The first excited state can be reached by exciting the β-spin electron from HOMO-1 to one of HOMO, thereby giving the term symbol of ^3E. Consequently, in the CASSCF calculations, the active space was set as six electrons and eight molecular orbitals, denoted as CAS(6,8), to include transitions from the ground states to the first seven excited states in the calculations. The less costly computation CAS(4,7) was also conducted for comparison. In TD-DFT and CIS calculations, on the other hand, up to 64 excited states could be searched.

IV. RESULTS AND DISCUSSION

A. Excitation energies

Previous spectroscopic studies have established that the ZPL of the $^3A_2 \to {}^3E$ transition of the $(NV)^-$ defect center is located at 1.945 eV, while the vertical excitation energy ΔE (i.e., the absorption maximum) is 2.18 ± 0.05 eV at the liquid nitrogen temperature.[1,30] As summarized in Table I and Fig. 3, calculated vertical excitation energies of different model clusters vary quite markedly, even within the same level of theory and basis set. A possible account for the variation is that most clusters used in the calculations are not large enough to enclose completely the electron density
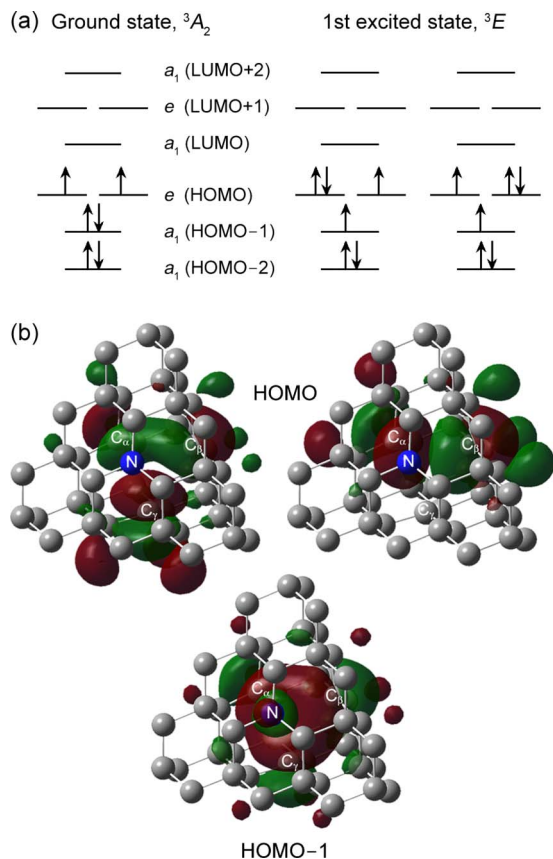
FIG. 2. (Color online) (a) Calculated electron configurations of the $(NV)^-$ center. The lowest excitation occurs as the β-spin electron in HOMO-1 transfers to HOMO. (b) Molecular orbital maps of HOMO and HOMO-1 calculated for $C_{49}(NV)^-H_{52}$ by CAS(6,8). In the structures superimposed on the orbital maps, the nitrogen and three carbon atoms surrounding the vacancy are labeled by N, C_α, C_β, and C_γ, respectively (surface hydrogen not shown). The electron densities are mainly distributed in the vacancy.

within the lattice. As a result, the electron density leakage out of the center and the surface hydrogen atoms significantly alter the electronic distribution of the defect. In the cases of larger and more spherically shaped model clusters, i.e., the sphere-like $C_{85}(NV)^-H_{76}$, $C_{89}(NV)^-H_{80}$, and $C_{104}(NV)^-H_{86}$, at least two complete carbon shells outside the defect centers are provided, effectively preventing the density leakage as well as the interference from surface atoms. A comparison of MO maps illustrated in Fig. 4 shows the obvious superiority of sphere-like $C_{85}(NV)^-H_{76}$ to $C_{24}(NV)^-H_{30}$ from this aspect. The ΔE values (and other transition properties) of these large clusters are therefore quite similar to each other, although their surface conformations differ. In contrast, the tetrahedron-like $C_{85}(NV)^-H_{76}$ cluster has a fewer number of carbon shells, resulting in an apparent bias in the calculation result. Since the calculated vertical excitation energies converge at the sphere-like $C_{85}(NV)^-H_{76}$, it leads to the conclusion that a model cluster containing two complete carbon shells around the defect center (yielding a model size of ~1.0 nm in diameter) is adequate to represent the $(NV)^-$ center in diamond.

It has been known that the calculated CIS excitation energies are systematically higher than the experimental ones.[43,44] Therefore, an excess of ~0.45 eV in the CIS-calculated energies shown in Table I comes of no surprise.

The CASSCF-calculated energies, on the other hand, are generally considered more accurate since nondynamical correlations for degenerate frontier orbitals are included in the calculations by the use of multiple configurations.[43,45] Unfortunately, because of limited computational resources, it is impractical at present to apply the CASSCF calculations to large clusters (>50 carbon atoms) even with a rather small active space, and the values calculated for small models were not satisfactory. In contrast, TD-DFT is expected to give a better estimation on the vertical excitation energy by virtue of the Kohn–Sham formalism which evaluates the virtual orbital energies more accurately than the HF algorithm.[44] As a result, relatively small deviations from the experimental value were obtained with TD-DFT.

In this work, the 6-31G(d) basis set has been extensively used. The use of the polarization function is believed to describe properly the lone pair electrons of the nitrogen atom as well as the dangling electrons of the three carbon atoms around the vacancy.[4,43,45] Moreover, since the $(NV)^-$ defect center is negatively charged, the diffuse function is also expected to be included in the calculations, and attempts have been made to use the 6-31+G(d) basis set. However, in applying the diffuse function to all atoms, we found that the calculations yielded surprisingly low excitation energies, e.g., $\Delta E < 1$ eV by CIS for small clusters (see Fig. 5). This marked underestimation is attributed to the fact that including more mobile electron densities in the calculations reinforces the density leakage and interference from the surface of these finite-sized clusters. Indeed, a recent study on molecules with various basis sets showed a systematic decrease in excitation energy when the diffuse function was introduced.[46]

A compromise to accommodate the calculation is to apply 6-31+G(d) only to the central atoms surrounding the vacancy, while all other atoms remain with 6-31G(d). A comparison of vertical excitation energies calculated by TD-DFT and CIS with/without the diffuse function in the basis set is sketched in Fig. 5. For small clusters such as $C_{24}(NV)^-H_{30}$ and $C_{33}(NV)^-H_{36}$, the introduction of the diffuse function spoiled ΔE and removed the degeneracy of the excited states since they were too small to prevent the density leakage and the surface interference from happening. For larger sphere-like ones such as $C_{85}(NV)^-H_{76}$ and $C_{104}(NV)^-H_{86}$, DFT calculations with this approach did not always lower the total energy of the optimized structure, making little improvement in ΔE with a much higher computational cost. In CIS calculations of these large clusters, on the other hand, we found a negligible variation in vertical excitation energies (differences caused by basis set in ΔE less than 0.01 eV) and other OPA properties when the diffuse function was employed on the central atoms, implying the negative charge rather localized in the center of the nitrogen-vacancy complex. Although the application of the 6-31+G(d) basis set on the whole large clusters yielded the CIS energies closer to the experimental value, this treatment is basically too expensive. As a result, we suggest that the choice of a large enough model is more essential than the

TABLE I. Computational results of the $^3A_2 \to {}^3E$ transition of the (NV)$^-$ defect center in diamond, where ΔE is the vertical excitation energy, $|\boldsymbol{\mu}|$ is the magnitude of the transition dipole moment, $a_{H-1 \to H}$ is the configuration interaction expansion coefficient for the first single excitation (i.e., the β-spin electron HOMO$-1 \to$ HOMO transition), and σ_{OPA} is the one-photon absorption cross section of the transition.

Species (conformation)	Method	Basis set	ΔE (eV)	$|\boldsymbol{\mu}|$ (debye)	$a_{H-1 \to H}$	σ_{OPA} [a] (10^{-17} cm^2)
C$_{24}$(NV)$^-$H$_{30}$ (disk)	TD-DFT	6-31G(d)	1.803	3.821	0.935	1.439
		6-31G(d)|6-31+G(d)	1.490	1.378[b]	0.999	$\cdots$ [b]
	CIS	6-31G(d)	2.115	4.598	0.912	2.415
		6-31G(d)|6-31+G(d)	1.316	0.624[b]	0.285[b]	$\cdots$ [b]
	CAS(4,7)	6-31G(d)	2.553	5.725	0.874	4.372
	CAS(6,8)	6-31G(d)	2.521	5.879	0.879	4.300
C$_{33}$(NV)$^-$H$_{36}$ (cuboid)	TD-DFT	6-31G(d)	1.737	3.386	0.963	1.092
		6-31G(d)|6-31+G(d)	1.556	3.647	0.951	1.146
	CIS	6-31G(d)	2.106	4.181	0.933	1.987
		6-31G(d)|6-31+G(d)	1.778	4.423	0.407[b]	1.900
	CAS(4,7)	6-31G(d)	2.532	6.123	0.870	4.728
	CAS(6,8)	6-31G(d)	2.480	6.367	0.876	4.726
C$_{49}$(NV)$^-$H$_{52}$ (tetrahedron)	TD-DFT	6-31G(d)	1.913	2.999	0.972	0.936
		6-31G(d)|6-31+G(d)	1.739	3.401	0.963	1.104
	CIS	6-31G(d)	2.308	3.802	0.914	1.792
		6-31G(d)|6-31+G(d)	2.056	4.049	<0.10 [b]	1.824
	CAS(4,7)	6-31G(d)	2.587	6.047	0.892	5.046
	CAS(6,8)	6-31G(d)	2.577	6.052	0.938	4.998
C$_{85}$(NV)$^-$H$_{76}$ (tetrahedron)	TD-DFT	6-31G(d)	1.761	2.809	0.972	0.761
		6-31G(d)|6-31+G(d)	1.566	3.314	0.967	0.952
	CIS	6-31G(d)	2.157	3.627	0.901	1.530
		6-31G(d)|6-31+G(d)	1.863	3.942	0.786	1.577
C$_{85}$(NV)$^-$H$_{76}$ (sphere)	TD-DFT	6-31G(d)	2.159	2.814	0.976	0.922
		6-31G(d)|6-31+G(d)	1.929	0.391[b]	0.993	$\cdots$ [b]
	CIS	6-31G(d)	2.649	3.584	0.792	1.813
		6-31G(d)|6-31+G(d)	2.640	3.574	<0.10 [b]	1.797
C$_{89}$(NV)$^-$H$_{80}$ (sphere)	TD-DFT	6-31G(d)	2.161	2.783	0.980	0.903
		6-31G(d)|6-31+G(d)	2.054	0.592[b]	0.985	$\cdots$ [b]
	CIS	6-31G(d)	2.639	3.564	0.790	1.778
		6-31G(d)|6-31+G(d)	2.630	3.546	<0.10 [b]	1.763
C$_{104}$(NV)$^-$H$_{86}$ (sphere)	TD-DFT	6-31G(d)	2.200	2.707	0.979	0.870
		6-31G(d)|6-31+G(d)	2.158	2.681	0.924	0.837
	CIS	6-31G(d)	2.681	3.547	0.723	1.723
		6-31G(d)|6-31+G(d)	2.670	3.480	0.244[b]	1.796
Average	TD-DFT[c]	6-31G(d)	2.17 ± 0.02	2.77 ± 0.04	$\cdots$	0.90 ± 0.02
	CIS[c]	6-31G(d)	2.66 ± 0.02	3.56 ± 0.01	$\cdots$	1.77 ± 0.03
	CAS(6,8)	6-31G(d)	2.53 ± 0.03	6.10 ± 0.18	$\cdots$	4.67 ± 0.25
Expt.[d]			2.18 ± 0.05	$\cdots$	$\cdots$	3.1 ± 0.8

[a]Off-resonance condition: Blueshifted from the vertical excitation by 0.15 eV.
[b]Apparent divergence due to discrepant arrangement of molecular orbitals.
[c]Average for the largest three sphere-like model clusters.
[d]Reference 30.

effort to push toward the complete basis set. A model size of ~100 carbon atoms is therefore desired, and the economical 6-31G(d) basis set is sufficient.

It would be queried if the quantum confinement effect prohibits the calculated energy gaps of these size-limited model clusters from comparing with the true situation in a bulk sample. For small hydrogenated diamond lattice clusters (pure diamondoids), previous DFT and quantum Monte Carlo studies showed a size threshold of ~1 nm above which the quantum confinement disappeared.[47,48] We have tested the vertical excitation energies of pure diamondoids consisted of 26, 51, 87, and 106 carbon atoms by TD-DFT/6-31G(d), obtaining ΔE of these clusters as 7.62, 7.21, 6.48, and 6.39 eV, respectively, whose trend of conver-

gence agreed with former theoretical investigations. On the other hand, we noticed that HOMOs of these pure diamondoids distributed throughout the whole carbon lattice, while those of model clusters with the (NV)$^-$ defect concentrated quite well in the center. The density decayed quickly outward from the center, in consistent with a recent report using DFT-LDA calculations with a supercell model.[21] Hence, the wave function of the defect should have little size dependence, consequently negligible or none of quantum confinement effect. We were convinced that the quantum confinement effect plays an unimportant role in our defect model clusters, at least in the largest ones (85 carbon atoms and above).

Table I summarizes the results of the computations at different levels of theory for clusters of various sizes, and
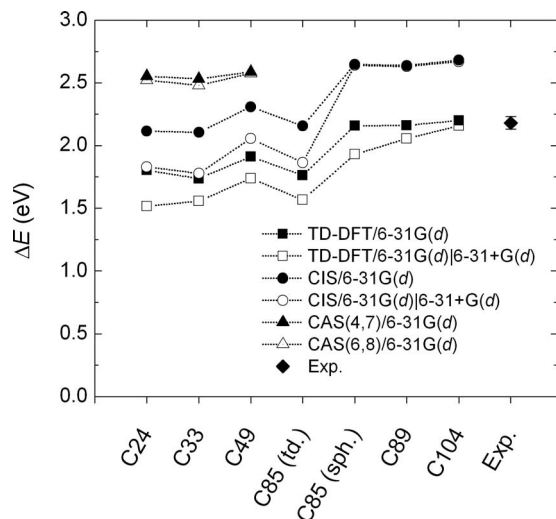
FIG. 3. Vertical excitation energies of the $^3A_2 \rightarrow {}^3E$ transition predicted by different computational methods and cluster models. The experimental absorption maximum is 2.18 ± 0.05 eV (Refs. [1] and [30]), shown as the rightmost data point on the plot.

FIG. 5. Basis set dependence of calculated vertical transition energies. Solid symbols: All atoms adopting the 6-31G(d) basis set (no diffuse function); open symbols: The additional diffuse function applied on the central atoms around the defect center; symbols with cross: All atoms adopting the diffuse function.

Fig. 3 illustrates the dependence of calculated vertical excitation energies on these factors. Specifically, the excitation energy obtained with the 6-31G(d) basis set by CAS(6,8) for smaller molecular cluster models is 2.53 ± 0.03 eV, and by CIS and TD-DFT for the largest three models are 2.66 ± 0.02 and 2.17 ± 0.02 eV, respectively.

B. OPA cross sections

As shown in Eq. (7), the OPA cross section is a function of the excitation angular frequency ω, the transition dipole moment **R**, and the distribution function $\Sigma_{v'} |\langle \Theta_{fv'} | \Theta_{i0} \rangle|^2 D(\omega_{fv',i0} - \omega, \gamma_{fv',i0})$. Experimentally, the OPA cross section of the (NV)$^-$ center has been determined by Wee *et al.*[30] to be $\sigma_{OPA} = (3.1 \pm 0.8) \times 10^{-17}$ cm^2 at 532 nm. This wavelength corresponds to the excitation energy of 2.33 eV, which is 0.15 eV blueshifted from the measured vertical excitation energy of 2.18 eV.[1,30] In order to make direct comparison between our calculation and their measurement, we fixed the off-resonance condition at $\hbar\omega_{OPA} = \Delta E + 0.15$ eV and therefore determine the excitation angular frequency ω used for each model in the computation.
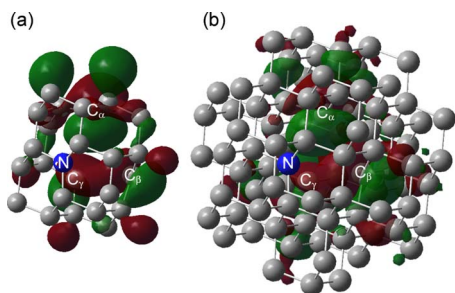

FIG. 4. (Color online) Comparison of HOMO density distributions of (a) C$_{24}$(NV)$^-$H$_{30}$ and (b) sphere-like C$_{85}$(NV)$^-$H$_{76}$ (surface hydrogen atoms not shown). There are severe density leakage and surface interference in small clusters, while the density is well enclosed in the defect center in large models.
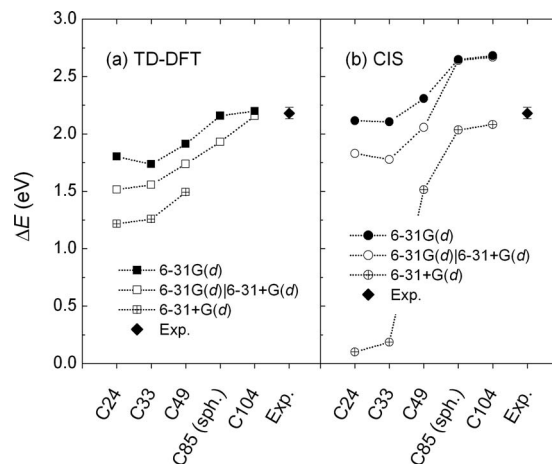
The refractive index of $n_e = 2.426$ at the excitation wavelength has been reported.[15] Although the true refractive indices of these small model clusters, being different from the bulk crystal, are unknown, the adoption of the bulk value is reasonable since we were attempting to compare to experimental findings from bulk samples. Now the evaluation of OPA cross sections can be made if the transition dipole moments and the associated distribution function are known. The former can be obtained directly from computational results; the remaining unknown factor is the distribution function. To evaluate this function at the particular excitation energy $\hbar\omega_{OPA}$, one has to know all Franck–Condon factors and Lorentzian lineshape functions corresponding to the individual vibronic transitions by either empirical simulation or computation. While direct computation of the excited state potential energy surface (PES) of the defect center is not achieved yet, we have instead modeled an empirical PES with the aid of experimental absorption and fluorescence spectra in a previous work.[17] With the information obtained therein, the distribution function at any excitation wavelength could be calculated and thus the whole absorption spectrum simulated. At the particular wavelength of 532 nm, a value of ~ 40 a.u. for the distribution function was estimated. There is yet another method to evaluate the distribution function, namely, to approximate it as a single Lorentzian function instead of a summation of many Lorentzian functions. This approach is valid since the spectral lineshapes are all roughly Lorentzian.[39] Taking $\hbar\gamma_{fi} = 0.20$ eV, a similar value of ~ 35 a.u. was obtained. Although the latter method was not adopted in the ensuing calculations of this work, such a treatment is useful in case that neither computed nor empirical PES of the molecular system is available.

In Table I we list the calculated transition dipole moments, the configuration interaction expansion coefficients of the HOMO$-1 \rightarrow$ HOMO transition involving the β-spin electron, and the OPA cross sections. Note that in these calculations, because the first excited state is doubly degenerate,
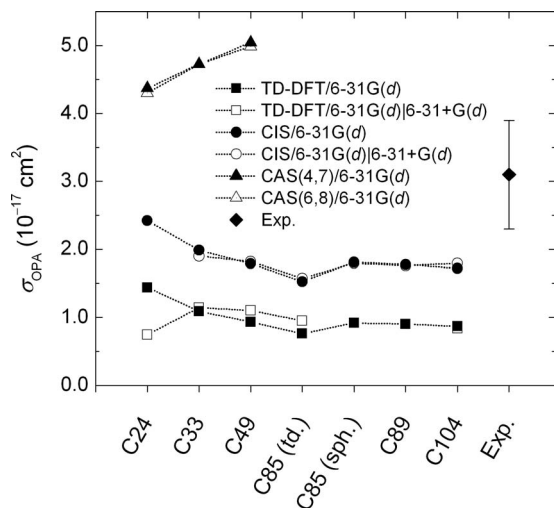
FIG. 6. OPA cross sections of the $^3A_2 \to {}^3E$ transition predicted by different computational methods and cluster models. A blueshift of 0.15 eV in the excitation energy from the vertical excitation was assumed in the calculation. Shown on the rightmost of the plot is the experimental value of $(3.1 \pm 0.8) \times 10^{-17}$ cm^2 (Ref. 30).

σ_{OPA} is twice the value obtained from Eq. (7). While the excited states lying above ^3E may also contribute to the absorption at 532 nm, their contributions are rather small and therefore ignored in this computation. Figure 6 summarizes the σ_{OPA} values of all calculations performed in this work. Compared to the experimental data from Ref. 30, the OPA cross sections calculated by TD-DFT are all severely underestimated, despite that their values are nearly independent of the cluster size. It might be associated with the undervaluation of transition dipole moments. This is not unreasonable, since the functional is aimed for optimal geometries but does not guarantee accurate transition properties.

The CIS-calculated results gave rise to σ_{OPA} $=(1.77 \pm 0.03) \times 10^{-17}$ cm^2 for the largest three sphere-like model clusters with the 6-31G(d) basis set. CIS is regarded as the most inexpensive theory which can obtain relatively accurate transition properties of systems up to several hundred first-row atoms,[44] and therefore the moderate underestimation is acceptable. The CASSCF calculation, in contrast, predicted a somewhat overestimated number, σ_{OPA} $=(4.67 \pm 0.25) \times 10^{-17}$ cm^2. At present, we cannot determine whether the predictions of CASSCF are perturbed by the surface effect since the calculations on larger clusters are unavailable.

Finally, we consider the basis set effect on the calculated σ_{OPA}. As mentioned above, applying the 6-31+G(d) basis set on the central atoms affects the stability of the model clusters in the TD-DFT calculations. Not only have the clusters become less stable but also the arrangement of the molecular orbitals and configuration interaction expansion coefficients are disturbed. The coefficients of the β-spin electron HOMO$-1 \to$ HOMO transition were typically 0.90 or higher, meaning a nearly pure one-electron transition and only one dominating configuration of the excited state.[44] However, in some cases the coefficients diverged due to incorrect arrangements of virtual molecular orbitals and hence yielded obvious errors in transition dipole moments and OPA

cross sections. This might occur in both TD-DFT and CIS computations. If such an event does not occur, the calculated values from both basis set were generally quite similar. Pondering the accuracy and computational cost, the 6-31G(d) basis set appears to be an adequate choice for further exploration.

C. TPA cross sections

According to Eq. (9), both the transition between initial (ground) and intermediate states and the transition between intermediate and final states participate in the TPA process. Moreover, for the noncentrosymmetric system, the intermediate state should include both initial and final states, meaning that in addition to the transition dipole moments, permanent dipole moments also contribute to the TPA cross sections.[35–37] The information of these dipole moments can be deduced from the CIS calculation in the GAUSSIAN 03 package and the CASSCF calculation in the MOLPRO package.

Experimentally, the TPA cross section of the $^3A_2 \to {}^3E$ transition in (NV)$^-$ was measured at 1064 nm, which is twice the wavelength employed in the OPA process.[30] Hence, the off-resonance condition was set at $2\hbar\omega_{TPA} = \Delta E + 0.15$ eV. As a result, the distribution functions described in Eqs. (7) and (20) have the same value under such settings. To exclude any approximation in evaluating the distribution function, the ratio $\sigma_{TPA}/\sigma_{OPA}$ was additionally calculated. This ratio serves to verify whether the transition dipole moments involved in OPA and TPA cross sections calculated under the same level of theory are in reasonable consistency.

It is informative to point out the number of intermediate states used in the calculation of σ_{TPA} and $\sigma_{TPA}/\sigma_{OPA}$ by each method. In CIS, up to 64 states were taken into account for smaller model clusters such as C$_{24}$(NV)$^-$H$_{30}$ and C$_{33}$(NV)$^-$H$_{36}$. While taking this large number of intermediate states into account is impractical for larger clusters or the CASSCF computation, we found that the first several states (mainly the ground state and the doubly degenerate first excited states) already contribute more than 90% of the weight in the transformed transition matrix elements that described in Eq. (18). As a result, as few as eight states are sufficient in practice, which makes possible the investigations on larger clusters containing more than 100 carbon atoms using CIS.

Table II list the computed TPA properties along with the experimental data. The refractive index of $n_e = 2.393$ was estimated at the excitation wavelength of 1064 nm.[15] The variations of the calculated σ_{TPA} and $\sigma_{TPA}/\sigma_{OPA}$ with cluster size are illustrated in Fig. 7. As seen, the predictions of σ_{TPA} by CIS show a large variation with the cluster size and they are severely overestimated for smaller clusters. In addition, due to the underestimation of σ_{OPA} in CIS, the $\sigma_{TPA}/\sigma_{OPA}$ ratios are disappointingly large. The discrepancy lessens for larger clusters such as the sphere-like C$_{85}$(NV)$^-$H$_{76}$, where a much more acceptable result was achieved. In contrast to CIS, the CASSCF calculations yielded fairly reasonable σ_{TPA} values and surprisingly good $\sigma_{TPA}/\sigma_{OPA}$ ratios for clusters of less than 50 carbon atoms.

The origin of the discrepancy (about a factor of 2 to 3 difference) in σ_{TPA} between computation and experiment is

TABLE II. Two-photon absorption cross sections (σ_{TPA}) calculated for the $^3A_2 \rightarrow {}^3E$ transition of the (NV)$^-$ defect center in diamond.

Species (conformation)	Method	Basis set	σ_{TPA}, linear polarization[a] (10^{-50} cm^4 s)	σ_{TPA}, circular Polarization (10^{-50} cm^4 s)	$\sigma_{TPA}/\sigma_{OPA}$ (10^{-33} cm^2 s)
C$_{24}$(NV)$^-$H$_{30}$ (disk)	CIS	6-31G(d)	6.160	3.632	2.551
		6-31G(d)|6-31+G(d)	$\cdots$ [b]	$\cdots$	$\cdots$
	CAS(4,7)	6-31G(d)	1.099	1.638	0.251
	CAS(6,8)	6-31G(d)	1.099	1.595	0.256
C$_{33}$(NV)$^-$H$_{36}$ (cuboid)	CIS	6-31G(d)	4.145	5.002	2.086
		6-31G(d)|6-31+G(d)	3.979	5.191	2.095
	CAS(4,7)	6-31G(d)	1.194	1.765	0.253
	CAS(6,8)	6-31G(d)	1.238	1.788	0.262
C$_{49}$(NV)$^-$H$_{52}$ (tetrahedron)	CIS	6-31G(d)	2.187	1.904	1.211
		6-31G(d)|6-31+G(d)	3.001	4.121	1.645
	CAS(4,7)	6-31G(d)	1.795	2.692	0.356
	CAS(6,8)	6-31G(d)	1.717	2.574	0.344
C$_{85}$(NV)$^-$H$_{76}$ (tetrahedron)	CIS	6-31G(d)	2.715	3.474	1.774
		6-31G(d)|6-31+G(d)	3.755	5.121	2.380
C$_{85}$(NV)$^-$H$_{76}$ (sphere)	CIS	6-31G(d)	1.331	1.721	0.734
		6-31G(d)|6-31+G(d)	1.257	1.630	0.700
C$_{89}$(NV)$^-$H$_{80}$ (sphere)	CIS	6-31G(d)	1.278	1.640	0.719
		6-31G(d)|6-31+G(d)	1.231	1.597	0.698
C$_{104}$(NV)$^-$H$_{86}$ (sphere)	CIS	6-31G(d)	1.110	1.437	0.644
		6-31G(d)|6-31+G(d)	0.686[b]	0.978	0.382
Average	CIS[c]	6-31G(d)	1.24 ± 0.09	1.60 ± 0.11	0.70 ± 0.04
	CAS	6-31G(d)	1.35 ± 0.24	1.99 ± 0.39	0.29 ± 0.04
Expt.[d]			0.45 ± 0.23	$\cdots$	0.15 ± 0.08

[a]Off-resonance condition: Blueshifted from the vertical excitation by 0.15 eV.
[b]Apparent divergence due to discrepant arrangement of molecular orbitals.
[c]Average for the largest three sphere-like model clusters.
[d]Reference 30.

manyfold. They are partly associated with the simplification in our mathematical formulas as well as the restriction in our computational methods. For example, we adopted the Placzek approximation when deriving Eq. (9), where all vibrational levels in the two-photon transition matrix elements have been ignored. Additionally, in treating the transition dipole moments and the two-photon transition matrix elements, all vibronic terms have been omitted (i.e., the Condon approximation) for simplicity and also for saving computational resources. Should this information be ignored, one has to make much more efforts to include all of them.[49,50] However, this is yet unachievable since the excited state PES has not been computed. As for the intrinsic constraints in the computational methods, CIS is known deficient since it takes into account only single excitations; while CASSCF considers all possible configurations, the active space is quite restricted in our calculations.[43] Furthermore, the possible long-range interactions, whether between two nearest neighboring (NV)$^-$ centers or between the center and a counterion (probably a positively charged nitrogen atom somewhere),[2,22,39] could not be considered in our size-limited models.

Despite the mathematical simplification and the computational limitation, we could still broadly compare our results to experimental measurements. With the 6-31G(d) basis set, an average σ_{TPA} of $(1.35 \pm 0.24) \times 10^{-50}$ cm^4 s per photon was predicted by CAS(6,8) for smaller clusters and $(1.24 \pm 0.09) \times 10^{-50}$ cm^4 s per photon by CIS for larger clusters, both of which were not far from the experimental value of $\sigma_{TPA}=(0.45 \pm 0.23) \times 10^{-50}$ cm^4 s per photon, ob-
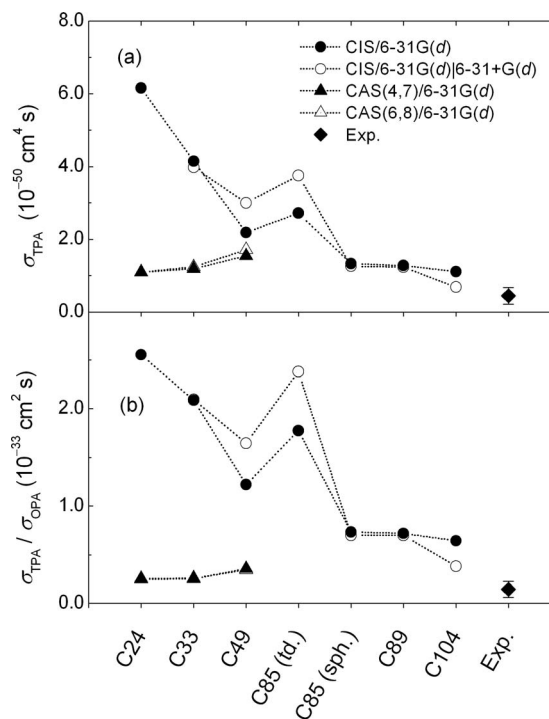

FIG. 7. (a) TPA cross sections and (b) TPA/OPA cross section ratios of the $^3A_2 \rightarrow {}^3E$ transition predicted by different computational methods and cluster models. In addition to the assumption of a blueshift of 0.15 eV in the excitation energy from the vertical excitation, linear polarization and single-beam excitation were also assumed in the calculation. The experimental TPA cross section is $(0.45 \pm 0.23) \times 10^{-50}$ cm^4 s (Ref. 30), shown as the rightmost data point in the upper panel.

tained using linearly polarized light at 1064 nm.[30] A merit of the calculation is that it provided the σ_{TPA} values if the excitation light source is circularly polarized, too, which were predicted to be about 30%–50% larger than the corresponding σ_{TPA} in linear polarization. In addition, in case a two-color—two-photon setup is used, the absorption cross sections can also be estimated accordingly. These values await to be verified in future experiments. We should also address that while CIS is a relatively inexpensive method, we do not expect a perfect accuracy but think it is reliable to a certain extent, e.g., a systematic overestimation within a factor of 3.

V. SUMMARY AND CONCLUSIONS

We have applied CIS, CASSCF, and TD-DFT calculations with the 6-31G(d) basis set to characterize the electronic excitation $^3A_2 \rightarrow \,^3E$ of the negatively charged nitrogen-vacancy defect center, (NV)⁻, in diamond. In these calculations, hydrogenated diamondoid clusters with a size of up to ∼100 carbon atoms were used to simulate the local environment of the defect center. Our results show that the vertical excitation energy, OPA, and TPA cross sections predicted by the CASSCF calculation are in rough agreement with the corresponding experimental values, mainly because the method is only applicable to small-sized clusters (<50 carbon atoms). In contrast, the application of TD-DFT and CIS calculations to larger clusters (up to ∼100 carbon atoms) can reproduce satisfactorily the vertical excitation energies of the transition and broadly the TPA cross sections of the defect center, respectively. While further improvement of the computational accuracy is needed, the present study using finite size models and relatively low-cost levels of theory provides an important theoretical framework for understanding of the optical properties of the (NV)⁻ center in diamond. The strategy developed in this work is eligible for systematic theoretical characterization of other point defects, e.g., the H3 and N3 centers, in diamond as well.

ACKNOWLEDGMENTS

[1] G. Davies and M. F. Hamer, Proc. R. Soc. London, Ser. A **348**, 285 (1976).
[2] Y. Mita, Phys. Rev. B **53**, 11360 (1996).
[3] A. Gruber, A. Dräbenstedt, C. Tietz, L. Fleury, J. Wrachtrup, and C. von Borczyskowski, Science **276**, 2012 (1997).
[4] J. H. N. Loubser and J. A. van Wyk, Rep. Prog. Phys. **41**, 1201 (1978).
[5] A. T. Collins, M. F. Thomaz, and M. I. B. Jorge, J. Phys. C **16**, 2177 (1983).
[6] D. A. Redman, S. Brown, R. H. Sands, and S. C. Rand, Phys. Rev. Lett. **67**, 3420 (1991).
[7] D. Redman, Q. Shu, A. Lenef, and S. C. Rand, Opt. Lett. **17**, 175 (1992).
[8] S. C. Rand, in *Properties and Growth of Diamond*, edited by G. Davies, EMIS Datareviews Series No. 9 (INSPEC, The Institute of Electrical Engineers, London, 1994), Chap. 7.4.
[9] A. Lenef, S. W. Brown, D. A. Redman, S. C. Rand, J. Shigley, and E. Fritsch, Phys. Rev. B **53**, 13427 (1996).
[10] A. Dräbenstedt, L. Fleury, C. Tietz, F. Jelezko, S. Kilin, A. Nizovtzev, and J. Wrachtrup, Phys. Rev. B **60**, 11503 (1999).
[11] F. Jelezko, C. Tietz, A. Gruber, I. Popa, A. Nizovtsev, S. Kilin, and J. Wrachtrup, Single Mol. **2**, 255 (2001).
[12] T. Gaebel, M. Domhan, C. Wittmann, I. Popa, F. Jelezko, J. Rabeau, A. Greentree, S. Prawer, E. Trajkov, P. R. Hemmer, and J. Wrachtrup, Appl. Phys. B: Lasers Opt. **82**, 243 (2006).
[13] N. B. Manson, J. P. Harrison, and M. J. Sellars, Phys. Rev. B **74**, 104303 (2006).
[14] N. B. Manson and R. L. McMurtrie, J. Lumin. **127**, 98 (2007).
[15] A. M. Zaitsev, *Optical Properties of Diamond* (Springer-Verlag, Berlin, 2001).
[16] S. Y. Kilin, A. P. Nizovtsev, T. M. Maevskaya, A. Dräbenstedt, and J. Wrachtrup, J. Lumin. **86**, 201 (2000).
[17] C.-K. Lin, H.-C. Chang, and S. H. Lin, J. Phys. Chem. A **111**, 9347 (2007).
[18] J. P. Goss, R. Jones, S. J. Breuer, P. R. Briddon, and S. Öberg, Phys. Rev. Lett. **77**, 3041 (1996).
[19] M. Łuszczek, R. Laskowskib, and P. Horodecki, Physica B (Amsterdam) **348**, 292 (2004).
[20] V. A. Pushkarchuk, S. Y. Kilin, A. P. Nizovtsev, A. L. Pushkarchuk, V. E. Borisenko, C. von Borczyskowski, and A. B. Filonov, Opt. Spectrosc. **99**, 245 (2005).
[21] A. Gali, M. Fyta, and E. Kaxiras, Phys. Rev. B **77**, 155206 (2008).
[22] J. A. Larsson and P. Delaney, Phys. Rev. B **77**, 165201 (2008).
[23] S.-J. Yu, M.-W. Kang, H.-C. Chang, K.-M. Chen, and Y.-C. Yu, J. Am. Chem. Soc. **127**, 17604 (2005).
[24] C.-C. Fu, H.-Y. Lee, K. Chen, T.-S. Lim, H.-Y. Wu, P.-K. Lin, P.-K. Wei, P.-H. Tsao, H.-C. Chang, and W. Fann, Proc. Natl. Acad. Sci. U.S.A. **104**, 727 (2007).
[25] Y.-R. Chang, H.-Y. Lee, K. Chen, C.-C. Chang, D.-S. Tsai, C.-C. Fu, T.-S. Lim, Y.-K. Tzeng, C.-Y. Fang, C.-C. Han, H.-C. Chang, and W. Fann, Nat. Nanotechnol. **3**, 284 (2008).
[26] A. M. Schrand, H. Huang, C. Carlson, J. J. Schlager, E. Ōsawa, S. M. Hussain, and L. Dai, J. Phys. Chem. B **111**, 2 (2007).
[27] L.-C. L. Huang and H.-C. Chang, Langmuir **20**, 5879 (2004).
[28] A. Krüger, Y. Liang, G. Jarre, and J. Stegk, J. Mater. Chem. **16**, 2322 (2006).
[29] A. Krüger, Angew. Chem., Int. Ed. **45**, 6426 (2006).
[30] T.-L. Wee, Y.-K. Tzeng, C.-C. Han, H.-C. Chang, W. Fann, J.-H. Hsu, K.-M. Chen, and Y.-C. Yu, J. Phys. Chem. A **111**, 9379 (2007).
[31] S. C. Lawson, D. Fisher, D. C. Hunt, and M. E. Newton, J. Phys.: Condens. Matter **10**, 6171 (1998).
[32] G. Davies, Physica B (Amsterdam) **273–274**, 15 (1999).
[33] K. K. Liang, R. Chang, M. Hayashi, and S. H. Lin, *Principle of Molecular Spectroscopy and Photochemistry* (National Chung Hsing University Press, Taichung, 2001), Chaps. 2 and 5.
[34] S. H. Lin, Y. Fujimura, H. J. Neusser, and E. W. Schlag, *Multiphoton Spectroscopy of Molecules* (Academic, New York, 1984), Chaps. 2 and 4.
[35] B. Dick and G. Hohlneicher, J. Chem. Phys. **76**, 5755 (1982).
[36] W. J. Meath and E. A. Power, J. Phys. B **17**, 763 (1984).
[37] B. N. Jagatap and W. J. Meath, J. Opt. Soc. Am. B **19**, 2673 (2002).
[38] D. P. Craig and T. Thirunamachandran, *Molecular Quantum Electrodynamics − An Introduction to Radiation-Molecule Interactions* (Academic, London, 1984), Chap. 5.
[39] K. Ohta and K. Kamada, J. Chem. Phys. **124**, 124303 (2006).
[40] K. Ohta, L. Antonov, S. Yamada, and K. Kamada, J. Chem. Phys. **127**, 084504 (2007).
[41] M. J. Frisch, G. W. Trucks, H. B. Schlegel, *et al.* GAUSSIAN 03, Revision C.2, Gaussian, Inc., Pittsburgh PA, 2003.
[42] MOLPRO, a package of *ab initio* programs written by H.-J. Werner, P. J. Knowles, R. Lindh *et al.*
[43] C. J. Cramer, *Essentials of Computational Chemistry: Theories and Models* (Wiley, Chichester, 2002), Chaps. 7 and 14.
[44] A. Dreuw and M. Head-Gordon, Chem. Rev. (Washington, D.C.) **105**, 4009 (2005).
[45] F. Jensen, *Introduction to Computational Chemistry* (Wiley, Chichester, 2007), Chaps. 4 and 5.
[46] C. B. Nielsen, S. Rettrup, and S. P. A. Sauer, J. Chem. Phys. **124**, 114108 (2006).
[47] J.-Y. Raty, G. Galli, C. Bostedt, T. W. van Buuren, and L. J. Terminello, Phys. Rev. Lett. **90**, 037401 (2003).
[48] N. D. Drummond, A. J. Williamson, R. J. Needs, and G. Galli, Phys. Rev. Lett. **95**, 096801 (2005).
[49] Y. J. Shiu, M. Hayashi, A. M. Mebel, Y.-T. Chen, and S. H. Lin, J. Chem. Phys. **115**, 4080 (2001).
[50] N. Lin, X. Zhao, A. Rizzo, and Y. Luo, J. Chem. Phys. **126**, 244509 (2007).